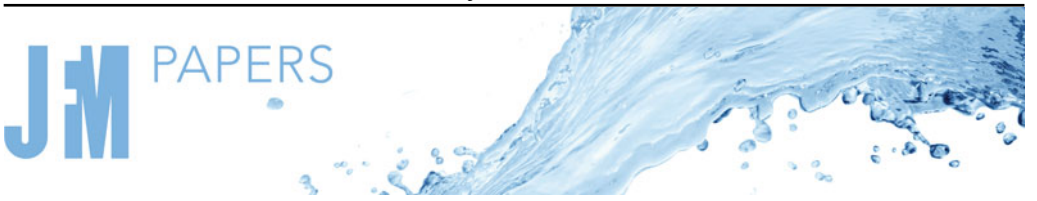
J. Fluid Mech. (2026), *vol.* 1040, A45, doi:10.1017/jfm.2026.11880



Impulse-induced liquid jets from bubbles with arbitrary contact angles

Hiroyuki Miyoshi[1], **Hiroya Watanabe**[2], **Ishin Kikuchi**[2] and **Yoshiyuki Tagawa**[2]

[1]Department of Mathematical Engineering and Information Physics, The University of Tokyo, 7-3-1, Hongo, Bunkyo-ku, Tokyo, Japan

[2]Department of Mechanical Systems Engineering, Tokyo University of Agriculture and Technology, 2-24-16, Naka-cho, Koganei, Tokyo 184-8588, Japan

Corresponding author: Hiroyuki Miyoshi, hiroyukimiyoshi@g.ecc.u-tokyo.ac.jp

(Received 3 February 2026 UTC; revised 24 June 2026 UTC; accepted 29 June 2026 UTC)

This paper investigates the relationship between the contact angle of a spherical bubble attached to a tube submerged in a container and the jet speed induced by an impulsive acceleration at its base. While it has been well established that bubble geometry strongly influences the ejection speeds of liquid jets, mathematical studies of liquid jets with arbitrary bubble shapes remain limited. In this work, we derive a pressure impulse in the small-cavity limit as a tractable integral of classical Legendre functions. It is shown that the jet speed can be divided into two components: (i) the velocity induced by the hydrostatic pressure impulse distribution created by the curvature of the bubble, and (ii) the velocity induced by the distribution of the submersion of the tube in a container. This decomposition reveals that an optimal bubble curvature emerges only when the tube is submerged: the optimality is absent for non-submerged configurations, where the jet speed increases monotonically with bubble depth. Experiments confirm this non-monotonicity and quantitatively support the predicted shift of the optimal geometry with submersion depth.

Key words: jets, general fluid mechanics, breakup/coalescence

1. Introduction

Liquid jets underpin a wide range of engineering applications, from precision manufacturing to high-resolution inkjet technologies (Lohse 2022). Eggers & Villermaux

© The Author(s), 2026. Published by Cambridge University Press. This is an Open Access article, distributed under the terms of the Creative Commons Attribution licence (https://creativecommons.org/licenses/by/4.0/), which permits unrestricted re-use, distribution and reproduction, provided the original article is properly cited.

https://doi.org/10.1017/jfm.2026.11880 Published online by Cambridge University Press

(2008) provide a comprehensive synthesis of the governing physics and canonical models in their seminal review, which continues to guide both fundamental and applied studies of liquid jets. The same physical principles have advanced industrial applications such as needle-free drug delivery (Baxter & Mitragotri 2006; Mohizin & Kim 2023; Srivastava *et al.* 2025), additive manufacturing and microfluidic actuation. Engineering applications such as tissue incision, metal cutting and precision cleaning demand rapidly accelerating jets that can be produced without elaborate apparatus (Tagawa *et al.* 2012).

Liquid jets form due to impulsive forcing. When a fluid confined by rigid boundaries experiences a sudden acceleration, the resulting flow can become strongly focused, particularly in the presence of cavities or bubbles. This flow focusing leads to high-speed liquid jets. Several studies have examined the formation of liquid jets. For instance, Bartolo *et al.* (2006) studied jet bursts due to the cavity collapse of droplets deformed by impulses between the droplets and hydrophobic surfaces. Several studies have modelled the dynamics of such high-speed jets. Gekle *et al.* (2009) formulated an axisymmetric potential model that links cavity collapse to jet velocity. Tagawa *et al.* (2012) examined the conditions required to form highly focused jets, while Rohilla and others investigated how geometric parameters affect the dynamics of jets by using electrical sparks to produce bubble cavitation (Rohilla & Marston 2023). Antkowiak *et al.* (2007) derived a semi-analytical solution for the velocity ejected from a spherical cavity after impulsive forcing under mixed boundary conditions. More recently, Dixit *et al.* (2025) showed that incorporating polymers into the liquid within spherical cavities can sustain even higher jet speeds by leveraging viscoelastic stresses. When the acceleration of a liquid occurs within a short time, it is useful to consider the limiting case of an impulsive change (Batchelor 2000). In such scenarios, a pressure impulse induced by an impulse satisfying the Laplace equation is used to investigate the dynamics of liquid jets. Philippi *et al.* (2018) showed that the flow induced by such a pressure impulse reduces to the solution of a Laplace problem with Dirichlet and Neumann boundary conditions in hemispherical fluid regions. Recent experiments by Kurihara *et al.* (2025) further demonstrated that under short-time acceleration, pressure fluctuations inside the liquid are strongly localised in time and can be quantitatively characterised within the pressure impulse framework, providing experimental support for the applicability of such modelling to impact-driven jet formation.

The mathematical modelling of Antkowiak *et al.* (2007) has been validated through liquid jet experiments. Onuki *et al.* (2018) invented an apparatus for generating highly-focused liquid jets using a submerged gas–liquid interface inside a tube. They showed that the submerged liquid dramatically increases the speed of jets, and that the speed increases as the level of submersion increases. By refining the jet apparatus used by Onuki *et al.* (2018), Kamamoto *et al.* (2021) and Kobayashi *et al.* (2024) developed a novel coating technology with highly viscous jets. Kiyama *et al.* (2016) conducted a series of experiments to identify important factors affecting the liquid jet speed. Watanabe *et al.* (2025) compared full numerical results for a pressure impulse in a tapered container with results obtained using a simplified model. It was determined that the jet velocity depends on both the total flow rate due to changes in the cross-sectional area of the container and changes in the pressure impulse along the centreline. It has also been reported that with regard to the experiment by Antkowiak *et al.* (2007), the bounce height due to the pressure impulse in a rotational container is dramatically lower than that in an irrotational container (Andrade *et al.* 2023; Xie 2025).

It is also widely known that the shape of a spherical cavity at the impulse time significantly affects the velocity of jets from the cavity (Gordillo & Blanco-Rodríguez 2023). The geometry of the liquid container also significantly affects jet speed and jet

https://doi.org/10.1017/jfm.2026.11880 Published online by Cambridge University Press

stability. Reuter & Ohl (2021) studied the supersonic jets from conical liquid containers and found that the jet speed increases as the cone angle increases. Krishnan *et al.* (2022) found that the jet velocity scales with the geometric mean of two physical velocities: the impact velocity and the meniscus-deformation velocity scale. Cheng *et al.* (2024) studied impacts on free surfaces to investigate viscous effects on focused jet formation. Although there have been a number of experimental studies on the relationship between jet velocity and meniscus shape, as summarised above, such mathematical modelling remains limited.

In this paper, we address this gap by developing an analytical pressure impulse solution for impulsively generated liquid jets from spherical bubbles with arbitrary contact angles. We consider a configuration consisting of a thin tube inserted into a container, with a bubble of controllable curvature attached to its tip. When an impulsive impact is applied to the bottom of the container, a liquid jet is generated from the bubble and propagates upwards through the tube. Using toroidal coordinates, originally introduced for solving Dirichlet boundary value problems by Lebedev (1965), together with special function representations based on Legendre functions, we derive closed-form expressions for the pressure impulse and the resulting jet velocity in the small-bubble limit. Related formulations using toroidal coordinates have recently been applied to problems such as bubble evaporation (Popov 2005; Wilson & D'Ambrosio 2023) and the interaction of multiple bubbles on substrates (Masoud *et al.* 2021; Dombrovsky *et al.* 2025), demonstrating their versatility in free boundary problems.

A key outcome of the present analysis is that the jet velocity can be decomposed into two physically distinct contributions: (i) a curvature-induced focusing term associated with the bubble geometry, and (ii) a submersion-induced term arising from the pressure impulse redistribution imposed by the surrounding container. This decomposition reveals an optimal bubble shape that maximises the jet velocity when the tube is submerged. This effect does not arise in the absence of submersion, where the jet speed increases monotonically with bubble depth. Image-based impact experiments validate the theoretical predictions and confirm that the optimal geometry emerges from the competition between these two mechanisms.

This new solution provides a hybrid approach that accounts for the container boundary. The toroidal coordinates and cylindrical coordinates are mixed using a change of variables, and the solution is given by a series expansion of the basis obtained from even-number derivatives of the analytical solution derived in § 3. A key point that is often missed in intuitive interpretations is that submersion does not simply shift the hydrostatic impulse by an additive constant. Because the jet speed is set by the gradient of the pressure impulse, the submersion depth enters the velocity through a distinct harmonic component associated with the boundary condition at the free surface. This yields a natural decomposition of the jet speed into two contributions, which serves as the central organising principle of this paper.

Numerical results for jet speed as a function of angle show that there is an optimal angle that maximises the jet speed. This trend is validated in an actual experiment in which impacts on the bottom of a container of liquid are induced. Most importantly, the critical angle of a spherical bubble decreases when the tube is submerged in a liquid. This result indicates that the control of the shape of the spherical cavity is important for producing high-speed jets.

The rest of the paper is organised as follows. Section 2 formulates the problem after the impulse and derives a three-dimensional (3-D) axisymmetrical Laplace equation for a pressure impulse with mixed boundary conditions on the meniscus and the wall. Using toroidal coordinates, analytical formulas for the pressure impulse with a small-bubble limit are obtained in § 3. For a general region with a bubble, a superposition of the solution

https://doi.org/10.1017/jfm.2026.11880 Published online by Cambridge University Press

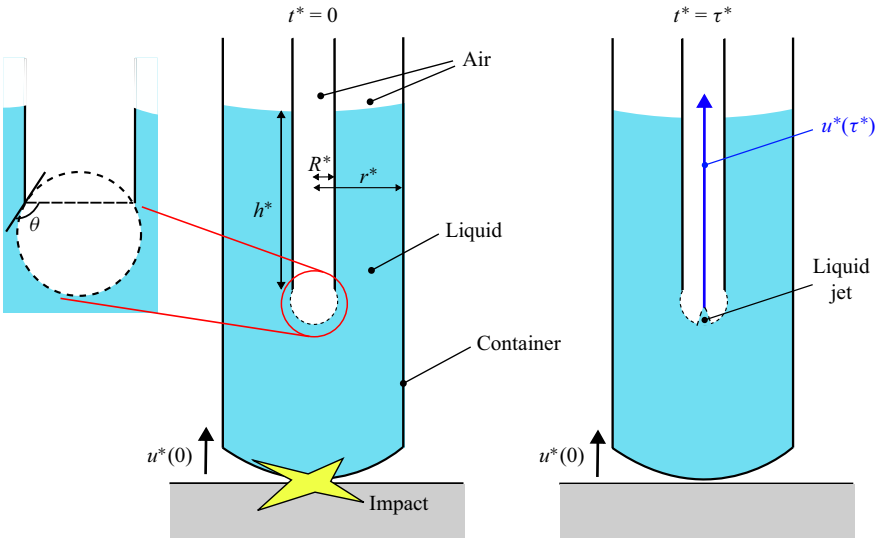


Figure 1. A liquid jet created by an impact on the ground. At the initial time $t^* = 0$, a falling container experiences an impact on its bottom, which produces a variation of the pressure impulse Π^* in a cylindrical container. The bubble region on the tip of the tube is assumed to be spherical, which is consistent with some experimental results (see Onuki *et al.* 2018). After the impact, a liquid jet is generated by the non-uniform distribution of the pressure impulse.

derived in § 3 with some derivatives is used to obtain the solution for the Laplace equation in § 4. Finally, the experimental results are presented in § 5, and discussions are given in § 6. Section 7 summarises our results.

2. Problem formulation

Throughout this paper, we use an asterisk to represent dimensional quantities. For non-dimensional quantities, we use normal letters. Consider a spherical bubble attached to the tip of a tube, where the tube is submerged to a depth h^* in a rigid container outside the tube. The container suddenly experiences an impulse at its bottom due to an impact, and the jet bursts from the bottom of the controlled spherical bubble. The angle between the meniscus of the bubble and the horizontal line is defined as θ. The radius of the cylindrical tube inside the container is R^*, and that of the container is r^*. Figure 1 shows a schematic of the geometric parameters.

We define the velocities before and after the impact as $\boldsymbol{u}^*(0)$ and $\boldsymbol{u}^*(\tau^*)$, where τ^* is an impact duration period. According to a classical result from Batchelor (2000) and work on liquid jets by Antkowiak *et al.* (2007), it is assumed that the fluid is inviscid and irrotational during the transient time of the impulse. The velocity of the liquid $\boldsymbol{u}^*$ is then governed by

$$\frac{\partial \boldsymbol{u}^*}{\partial t^*} = -\frac{1}{\rho^*}\nabla^* p^*, \tag{2.1}$$

where ∇^* is a dimensional gradient operator, p^* is a fluid pressure, and ρ^* is the density of the liquid. By integrating (2.1) with respect to the short time period of the impact τ^*,

https://doi.org/10.1017/jfm.2026.11880 Published online by Cambridge University Press

the velocity $\boldsymbol{u}^*(\tau^*)$ satisfies

$$\boldsymbol{u}^*(\tau^*) - \boldsymbol{u}^*(0) = -\frac{1}{\rho^*}\nabla^* \Pi^*. \tag{2.2}$$

Here, Π^* is the pressure impulse defined by the integral of the pressure p^* over the short impact duration τ^*. Since the flow is assumed to be incompressible, the pressure impulse Π^* satisfies the 3-D Laplace equation in the region filled with liquid, i.e.

$$\nabla^{*2}\Pi^* = 0 \tag{2.3}$$

in the cylindrical domain outside the bubble. The jet velocity $\boldsymbol{u}^*(\tau^*)$ is calculated using the spatial derivative of Π^*, as given in (2.2) after obtaining Π^*.

It is convenient to non-dimensionalise the pressure impulse and the coordinates, i.e. $\Pi^* = \Pi\ \rho^* U_0^* R^*$ and $(x^*, y^*, z^*) = (R^*x,\ R^*y,\ R^*z)$. With this scaling, the radius of the inner tube is always set to 1. Here, U_0^* is the velocity of the container in the z^*-direction at the initial time due to the elastic collision at the bottom. Furthermore, the non-dimensional geometric parameters are defined by $h := h^*/R^*$ and $\lambda := R^*/r^*$. The non-dimensional geometry is shown in figure 2(*a*).

Assuming axial symmetry of the shape of the cavity and container, it is convenient to study the jet speed in a cylindrical coordinate system defined by (ξ, z). We consider a general solution to the 3-D potential problem in a cylindrical region outside of a spherical cavity. The boundary of a spherical bubble with a contact angle θ is defined as

$$\mathcal{S} := \left\{ (\xi, z) \,\middle|\, \xi^2 + \left(z - \frac{1}{\tan\theta}\right)^2 = \frac{1}{\sin^2\theta},\ z \leqslant 0 \right\}. \tag{2.4}$$

Note that the depth of a bubble defined by H is related to the contact angle θ by

$$H = \tan(\theta/2). \tag{2.5}$$

We assume that the container length in the z-direction is much greater than the radius of the tube and the container. Hence the elastic collision on the bottom gives a uniform velocity distribution at $z \to -\infty$ after the impact.

The boundary condition for the interface is the Euler–Bernoulli equation at the free interface, which reduces to $\Pi = 0$ on the meniscus $\mathcal{S}$, and on the top of the liquid interface in the container at $1 < \xi < 1/\lambda$, $z = h$ (Onuki *et al.* 2018; Gordillo *et al.* 2020). Furthermore, assuming that the uniform gradient of the pressure impulse appears in the region above the bubble region, it is possible to approximate that the pressure impulse satisfies $\Pi = h$ on $z = 0$, $1 < \xi < 1/\lambda$. This assumption originates from the leading-order contribution to the pressure impulse Π from the surface on $z = h$, which is approximately constant and equal to $\Pi = h$, even in the vicinity of $\xi = 1$ and for $\theta > \pi/2$. This approximation was also adopted in previous work by Onuki *et al.* (2018), where it was shown to be in good agreement with experimental results for predicting jet velocities. For the side of the container, an impermeability condition is imposed, i.e. $\partial\Pi/\partial\xi = 0$ for $\xi = 1/\lambda$, $z < 0$, as the movement of the container is assumed to be only along the z-axis. As a result, the non-dimensional pressure impulse Π satisfies the following mixed boundary value problem in cylindrical coordinates:

https://doi.org/10.1017/jfm.2026.11880 Published online by Cambridge University Press

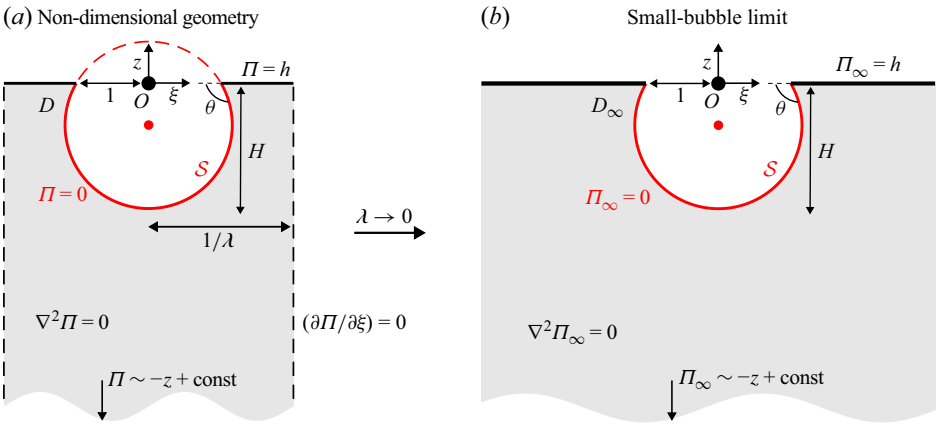


Figure 2. (*a*) The non-dimensional boundary value problem for a harmonic pressure impulse Π. (*b*) The geometry D_∞ in the small-bubble limit. When $\lambda \to 0$, the geometry is a semi-infinite half 3-D space outside a spherical-shaped bubble, denoted by D_∞. Note that H is related to θ as $H = \tan(\theta/2)$. The impulse Π is approximated well by Π_∞ as $\lambda \to 0$.

$$\begin{cases} \text{(i)} & \nabla^2 \Pi = 0, & (\xi, z) \in D, \\ \text{(ii)} & \dfrac{\partial \Pi}{\partial \xi}(1/\lambda, z) = 0, & z < 0, \\ \text{(iii)} & \Pi(\xi, z) = 0, & (\xi, z) \in \mathcal{S}, \\ \text{(iv)} & \Pi(\xi, 0) = h, & 1 \leqslant \xi \leqslant 1/\lambda, \\ \text{(v)} & \Pi(\xi, z) = -z + \text{const}, & z \to -\infty, \end{cases} \tag{2.6}$$

where the region D is the fluid region for $z < 0$, as shown in figure 2(*a*). After obtaining Π, the initial jet speed is calculated using the velocity at the bottom of the cavity with respect to the moving frame with (2.2).

3. The small-bubble limit

This section studies the small-bubble limit, i.e. when the cavity is sufficiently small compared to the radius of the container shown in figure 2(*a*). This case corresponds to the ratio of the radius of the inner tube to that of the container tending to 0, i.e. $\lambda \to 0$. The region is now a semi-infinite lower-half 3-D region outside the spherical bubble $\mathcal{S}$, denoted by D_∞. For this limiting case, it is possible to obtain an analytical solution for the field Π_∞ and thus the jet velocity induced by the impulsive acceleration.

As $\lambda \to 0$, the impermeability condition on the side wall in (2.6)(ii) vanishes. The pressure impulse defined by $\Pi_\infty(\xi, z)$ now satisfies

$$\begin{cases} \text{(i)} & \nabla^2 \Pi_\infty = 0, & (\xi, z) \in D_\infty, \\ \text{(iii)} & \Pi_\infty(\xi, z) = 0, & (\xi, z) \in \mathcal{S}, \\ \text{(iv)} & \Pi_\infty(\xi, 0) = h, & 1 \leqslant \xi \leqslant \infty, \\ \text{(v)} & \Pi_\infty(\xi, z) = -z + \text{const}, & z \to -\infty. \end{cases} \tag{3.1}$$

https://doi.org/10.1017/jfm.2026.11880 Published online by Cambridge University Press

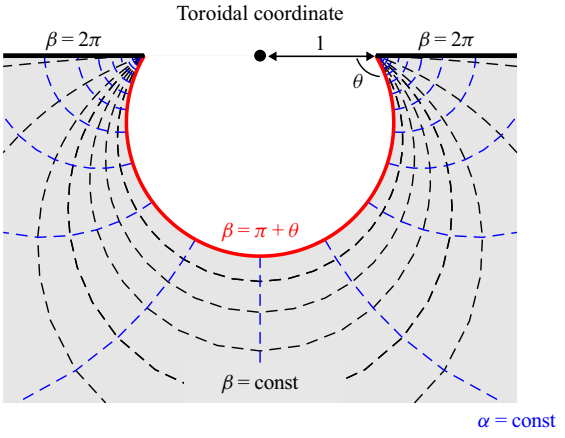


Figure 3. Toroidal coordinates (α, β) for solving the mixed boundary value problem for a pressure impulse Π_∞. Cylindrical coordinates (ξ, z) are mapped to the new coordinates (α, β) using the transformation in (3.2). The boundary of the bubble is expressed by $\beta = \pi + \theta$.

To solve the boundary value problem (3.1), it is convenient to change the cylindrical coordinates (ξ, z) to toroidal coordinates (α, β) (Lebedev 1965), where all boundaries of D_∞ can be expressed by a contour line in this coordinate system. Following a mathematical setting provided in Chapter 8 of Lebedev (1965), consider the change of variables

$$\xi(\alpha, \beta) = \frac{\sinh \alpha}{\cosh \alpha - \cos \beta}, \quad z(\alpha, \beta) = \frac{\sin \beta}{\cosh \alpha - \cos \beta}, \tag{3.2}$$

where the parameter spaces for α and β in the domain D_∞ are $0 < \alpha < \infty$, $\pi + \theta < \beta < 2\pi$. The inverse transform is given by

$$\alpha(\xi, z) = \frac{1}{2} \log \left(\frac{z^2 + (\xi + 1)^2}{z^2 + (\xi - 1)^2} \right), \quad \beta(\xi, z) = \pi + \tan^{-1} \left(\frac{2z}{\xi^2 + z^2 - 1} \right), \tag{3.3}$$

where β is chosen so that $\pi + \theta < \beta < 2\pi$. Using this coordinate system, the boundary of a spherical bubble $\mathcal{S}$ and the plane $1 < \xi$ with $z = 0$ correspond to $\beta = \pi + \theta$ and $\beta = 2\pi$, respectively. The correspondence between the geometry and parameters α and β is shown in figure 3. Using the new coordinates and the mathematical formulation in Lebedev (1965), the solution $\Pi_\infty(\xi, z)$ for the boundary value problem (3.1) is given by

$$\Pi_\infty(\xi, z) = \Pi_f(\xi, z) + h\Pi_g(\xi, z), \tag{3.4}$$

where

$$\Pi_f(\xi, z) := -z - f_\theta(\alpha(\xi, z), \beta(\xi, z)), \tag{3.5}$$

$$\Pi_g(\xi, z) := 1 - g_\theta(\alpha(\xi, z), \beta(\xi, z)), \tag{3.6}$$

and

$$f_\theta(\alpha, \beta) := 2\sqrt{2(\cosh \alpha - \cos \beta)} \int_0^\infty \tau \frac{\sinh(\theta\tau) \sinh[(2\pi - \beta)\tau]}{\cosh(\pi\tau) \sinh[(\pi - \theta)\tau]} P_{-(1/2)+\mathrm{i}\tau}(\cosh \alpha)\, \mathrm{d}\tau, \tag{3.7}$$

$$g_\theta(\alpha, \beta) := \sqrt{2(\cosh \alpha - \cos \beta)} \int_0^\infty \frac{\cosh(\theta\tau) \sinh[(2\pi - \beta)\tau]}{\cosh(\pi\tau) \sinh[(\pi - \theta)\tau]} P_{-(1/2)+\mathrm{i}\tau}(\cosh \alpha)\, \mathrm{d}\tau. \tag{3.8}$$

https://doi.org/10.1017/jfm.2026.11880 Published online by Cambridge University Press

The cylindrical coordinates (ξ, z) are related to (α, β) through the coordinate transformation (3.2). The function $P_\nu(z)$ is a special function called a Legendre function of the first kind with degree ν. The derivation of this formula is provided in detail in Appendix A.

Note that $\Pi_f(\xi, z)$ is a pressure impulse induced by the curvature of the spherical bubble with no submersion, and Π_g is a pressure impulse induced by the submersion of the tube. The total pressure impulse Π_∞ is decomposed into Π_f and Π_g times the submersion length h.

Although the expressions (3.7) and (3.8) are similar to (8.12.12) in Lebedev (1965), these solutions are novel due to the differing boundary conditions (i), (iii)–(v). This is also one of the main contributions of this paper.

This formula includes an integral of the function $P_{-(1/2)+\mathrm{i}\tau}(\cosh\alpha)$ with respect to τ. It is possible to calculate the function using some well-known integral representations (Lebedev 1965). Numerical computations for this function in our paper are given in Appendix B.

The speed of the jet is calculated directly using the derivative of Π_∞ in (3.4) with respect to z evaluated at the bottom of the bubble. To achieve this, the derivatives of f_θ and g_θ are calculated using the chain rule:

$$\frac{\partial f_\theta}{\partial z} = \frac{\partial \alpha}{\partial z}\frac{\partial f_\theta}{\partial \alpha} + \frac{\partial \beta}{\partial z}\frac{\partial f_\theta}{\partial \beta}, \quad \frac{\partial g_\theta}{\partial z} = \frac{\partial \alpha}{\partial z}\frac{\partial g_\theta}{\partial \alpha} + \frac{\partial \beta}{\partial z}\frac{\partial g_\theta}{\partial \beta}. \tag{3.9}$$

The jet speed is evaluated at the bottom of the spherical bubble located at $(\xi, z) = (0, -H)$. The parameters there are $\alpha = 0$ and $\beta = \pi + \theta$. Note that the derivatives of f_θ and g_θ with respect to α and β in (3.9) can be explicitly evaluated. For example, the derivative of g_θ with respect to β is given by

$$\begin{aligned}\frac{\partial g_\theta}{\partial \beta} = {} & \frac{\sin\beta}{\sqrt{2(\cosh\alpha - \cos\beta)}} \int_0^\infty \frac{\cosh(\theta\tau)\sinh[(2\pi-\beta)\tau]}{\cosh(\pi\tau)\sinh[(\pi-\theta)\tau]} P_{-(1/2)+\mathrm{i}\tau}(\cosh\alpha)\,\mathrm{d}\tau \\ & - \sqrt{2(\cosh\alpha - \cos\beta)} \int_0^\infty \tau \frac{\cosh(\theta\tau)\cosh[(2\pi-\beta)\tau]}{\cosh(\pi\tau)\sinh[(\pi-\theta)\tau]} P_{-(1/2)+\mathrm{i}\tau}(\cosh\alpha)\,\mathrm{d}\tau.\end{aligned} \tag{3.10}$$

By using the Mehler–Fock theorem and the integral representation of a Legendre function (Lebedev 1965), the speed at the bottom of the cavity $v_f(\theta)$ in a frame moving with the tube is given explicitly by

$$v_f(\theta) := \frac{\partial f_\theta}{\partial z}(0, \pi+\theta) = \sin^2\left(\frac{\theta}{2}\right) + 8\cos^3\left(\frac{\theta}{2}\right)\int_0^\infty \tau^2 \frac{\sinh(\theta\tau)\cosh[(\pi-\theta)\tau]}{\cosh(\pi\tau)\sinh[(\pi-\theta)\tau]}\,\mathrm{d}\tau \tag{3.11}$$

and

$$v_g(\theta) := \frac{\partial g_\theta}{\partial z}(0, \pi+\theta) = \frac{1}{2}\sin\theta + 4\cos^3\left(\frac{\theta}{2}\right)\int_0^\infty \tau \frac{\cosh(\theta\tau)\cosh[(\pi-\theta)\tau]}{\cosh(\pi\tau)\sinh[(\pi-\theta)\tau]}\,\mathrm{d}\tau. \tag{3.12}$$

Based on the pressure impulse decomposition (3.4), the total jet velocity $v(\theta)$ is then equal to

$$v(\theta) = v_f(\theta) + h\, v_g(\theta), \tag{3.13}$$

which means that the velocity is composed of the velocity $v_f(\theta)$ due to the pressure impulse of the impact with $h = 0$, and the velocity $v_g(\theta)$ caused by the pressure distribution due to the submergence of the tube. This is natural since the solution (3.4)

https://doi.org/10.1017/jfm.2026.11880 Published online by Cambridge University Press

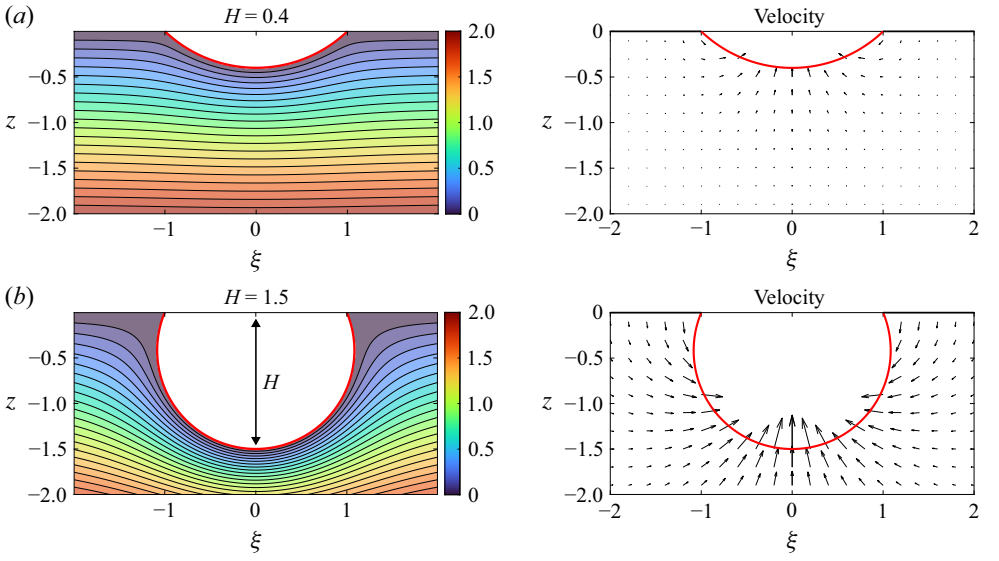


Figure 4. Contour plots for the harmonic pressure impulse $\Pi_f(\xi, z)$ in (3.5) and the velocity in (3.11), for (*a*) $H = 0.4$ and (*b*) $H = 1.5$. The value H is related to the angle θ as $H = \tan(\theta/2)$.

is composed of the hydrostatic pressure impulse due to the bubble Π_f and the pressure due to the submergence of the tube, which is Π_g times the height h. This decomposition is important because the jet speed $v(\theta)$ has a local maximum with respect to the bubble height $H = \tan(\theta/2)$ for fixed $h > 0$.

The final integrals in (3.11) and (3.12) do not appear to admit a simpler closed-form expression. However, since the integrand rapidly decays to zero as $\tau \to \infty$, they can be readily evaluated numerically. Nonetheless, it is possible to show that for $\theta = \pi/2$, the integral expression (3.11) can be simplified as follows:

$$v_f(\pi/2) = \frac{1}{2} + 2\sqrt{2}\int_0^\infty \tau^2 \frac{\cosh\left(\frac{\pi}{2}\tau\right)}{\cosh(\pi\tau)}\,\mathrm{d}\tau = 2. \tag{3.14}$$

This result corresponds to figure 6 in Antkowiak *et al.* (2007) as $\lambda \to 0$, where the jet produced from hemispherical bubbles was studied. This velocity is consistent with the fact that the pressure impulse for $H = 1$ ($\theta = \pi/2$) is explicitly written as $\Pi_f(\xi, z) = -z - z/(\xi^2 + z^2)^{3/2}$. It is easy to see that the function satisfies $\Pi_f(\xi, z) = 0$ on the lower hemisphere and $z = 0$, $\xi \geqslant 1$. This fact will be used in § 4. For $\theta = 0$, it is easy to see that $v_f(0) = 0$ and

$$v_g(0) = 4\int_0^\infty \frac{\tau\,\mathrm{d}\tau}{\sinh(\pi\tau)} = 8\int_0^\infty \frac{\tau\,\mathrm{d}\tau}{\mathrm{e}^{\pi\tau} - \mathrm{e}^{-\pi\tau}} = 8\lim_{\epsilon\to 0^+}\int_\epsilon^\infty \frac{\tau}{\mathrm{e}^{\pi\tau}}\sum_{n=0}^{\infty}\mathrm{e}^{-2n\pi\tau}\,\mathrm{d}\tau = 1. \tag{3.15}$$

Figure 4 shows contour plots of Π_f and velocity plots with cavity heights $H = 0.4$ and 1.5. Note that H and θ are related to each other by (2.5). As the cavity height H increases, the magnitude of the velocity increases. It can also be observed that the maximum velocity is attained at the bottom of the bubble. This is natural because the spherical bubble pushes as H increases, and the interval between contour lines becomes small, so that the pressure gradient at the bottom becomes large. For $h > 0$, the contour plots of Π_∞ and velocity

https://doi.org/10.1017/jfm.2026.11880 Published online by Cambridge University Press

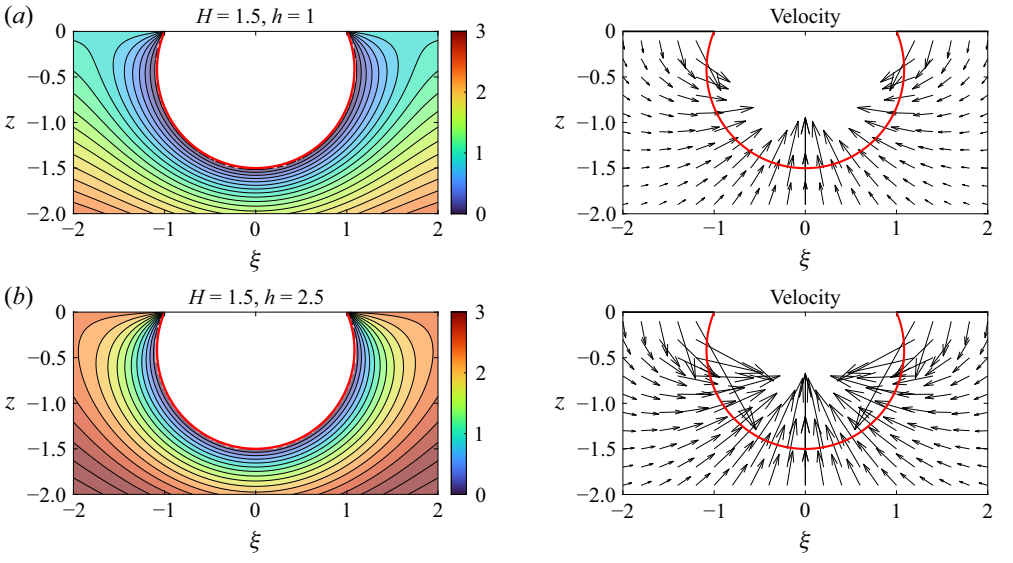


Figure 5. Contour plots for the harmonic pressure impulse $\Pi_\infty(\xi, z)$ in (3.4) and velocity in (3.13). Note that $\Pi_\infty(\pm 1, 0)$ is discontinuous due to the boundary conditions. Here, (*a*) $h = 1.0$ and (*b*) $h = 2.5$. The cavity height is fixed at $H = 1.5$.

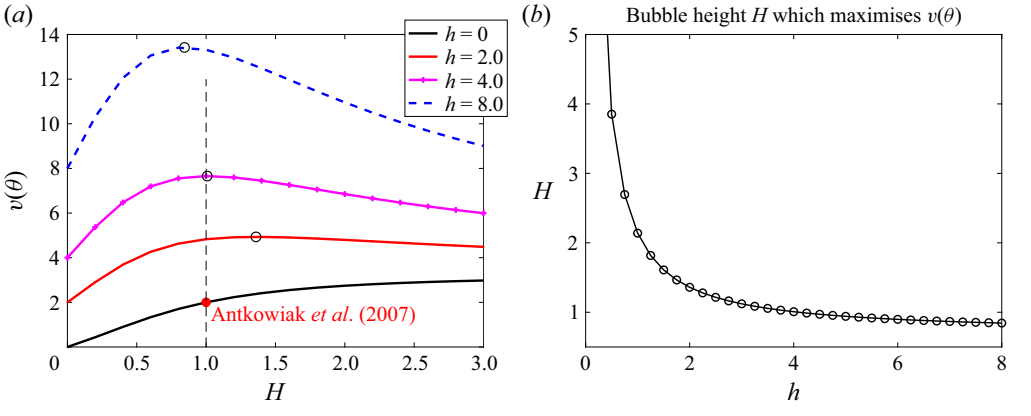


Figure 6. (*a*) The speed at the bottom of the bubble with different submersion depths h. The jet velocities with four different h values are examined, i.e. $h = 0, 2.0, 4.0, 8.0$. The circles correspond to the points where the velocity $v(\theta)$ is maximised. (*b*) The critical value of H that maximises the jet speed with respect to the depth h.

plots for cavity height $H = 1.5$ with $h = 1$ and 2.5 are shown in figure 5. The velocity becomes large as h increases.

Figure 6 shows the jet velocity $v(\theta)$ with respect to $H = \tan(\theta/2)$ for different submersion depths, $h = 0, 2.0, 4.0, 8.0$. For $h = 0$, the velocity monotonically increases as the height of the bubble H increases. On the contrary, for $h > 0$, there exists a critical value of H that maximises the velocity $v(\theta)$. It is also observed that the critical value of H gets smaller as h increases.

As shown in figure 6(*b*), the critical bubble height H converges as $h \to \infty$. According to the velocity decomposition (3.13),

https://doi.org/10.1017/jfm.2026.11880 Published online by Cambridge University Press

$$v(\theta) = v_f(\theta) + h\, v_g(\theta) \sim h\, v_g(\theta) \tag{3.16}$$

as h becomes large. This means that the bubble height that maximises $v(\theta)$ is obtained by maximising $v_g(\theta)$. Based on our numerical calculation, the value H converges to $H \sim 0.67$ as $h \to \infty$.

The formulas derived here work only when the walls and inner cavity are widely separated. When they are close, the jet velocity is not approximated well by the small-bubble limit. However, we will show that (3.7) and (3.8) are in good agreement with a wide range of parameter spaces of λ and H in the next section.

4. Exact solution for the pressure impulse using a series solution

Section 3 presents an analytical formula for the pressure impulse field and velocity when the bubble size is small enough to neglect the side wall effect. Although analytical formulas for the fields and velocities of liquid jets have been presented, the presence of the wall affects both. Antkowiak *et al.* (2007) studied the relationship between the jet velocity and changes in the cavity size and tube radius, where the contact angle of the cavity is always $\pi/2$. It was found, both numerically and experimentally, that the jet velocity decreases as the cavity approaches the wall boundary, i.e. $\lambda \to 1$. It was also observed that the velocity in the $h = 0$ case is approximately 1.

To study a situation similar to that in Antkowiak *et al.* (2007), we present a semi-analytical approach for obtaining the pressure impulse in the presence of a wall boundary based on the analytical formulas in § 3. Similar to the formulation in Antkowiak *et al.* (2007), the field inside the tube outside the spherical bubble is given by the superposition of high-order fields derived from the pressure impulse of (3.7) and (3.8).

4.1. *Derivation of the semi-analytical solution for $\theta = \pi/2$ by Antkowiak et al.*

Antkowiak *et al.* (2007) derived a semi-analytical solution for a potential problem in a tube outside a hemispherical bubble, i.e. $\theta = \pi/2$. They started the formulation by considering the initial function

$$\phi_0(\xi, z) := \frac{z}{(\xi^2 + z^2)^{3/2}}. \tag{4.1}$$

It is easy to see that $\Pi(\xi, z) := -z - \phi_0(\xi, z)$ satisfies the conditions (i), (iii)–(v) in (2.6). We consider the modified field $F_0(\xi, z) := \phi_0(\xi, z) + \psi_0(\xi, z)$, where $\psi_0(\xi, z)$ is added to satisfy the boundary condition (ii). By employing the condition $\psi_0(\xi, z) = 0$ on $z = 0$, $\psi_0(\xi, z)$ is represented by Fourier–sine functions with Bessel functions $I_0(\xi)$ as

$$\psi_0(\xi, z) := \int_0^\infty \eta_0(m) \sin(mz)\, I_0(m\xi)\, \mathrm{d}m, \tag{4.2}$$

where $\eta_0(m)$ is calculated from the Fourier–sine transform of the function to satisfy the boundary condition on the side wall of the tube:

$$\eta_0(m) = -\frac{2}{\pi} \int_{-\infty}^{0} \frac{\sin mz}{m\, I_1(m/\lambda)} \frac{\partial \phi_0}{\partial \xi}(1/\lambda, z)\, \mathrm{d}z. \tag{4.3}$$

Although $-z - F_0(\xi, z)$ is not an exact solution for the boundary value problem with a tube as $-z - F_0(\xi, z) \neq 0$ on $\mathcal{S}$, it is possible to obtain the solution using a new basis related to $\phi_0(\xi, z)$. Consider an even-number derivative of $\phi_0(\xi, z)$ with respect to z:

https://doi.org/10.1017/jfm.2026.11880 Published online by Cambridge University Press

$$\phi_{2n}(\xi, z) := \frac{1}{(2n)!}\frac{\partial^{2n}\phi_0}{\partial z^{2n}}(\xi, z), \quad \psi_{2n}(\xi, z) := \int_0^\infty \eta_{2n}(m)\sin(mz)\, I_0(m\xi)\,\mathrm{d}m, \tag{4.4}$$

where the coefficient $\eta_{2n}(m)$ is also calculated in a similar manner to (4.3) by simply modifying $\phi_0(1/\lambda, z)$ as $\phi_{2n}(1/\lambda, z)$. The solution $\Pi(\xi, z)$ is the superposition of the functions F_{2n}:

$$\Pi(\xi, z) := -z - \sum_{n=0}^{\infty} A_{2n}\, F_{2n}(\xi, z), \quad F_{2n}(\xi, z) := \phi_{2n}(\xi, z) + \psi_{2n}(\xi, z). \tag{4.5}$$

Antkowiak *et al.* (2007) derived an explicit representation for $F_{2n}(\xi, z)$ and then a linear system for the coefficients A_{2n}, with truncation order N.

We show that this approach is applicable to problems that do not always have a hemispherical bubble. The only modification is the basis function ϕ_{2n}.

4.2. *A semi-analytical solution for an arbitrary angle θ*

We start the formulation from the solution $\phi_0(\alpha, \beta) := f_\theta(\alpha, \beta)$ defined in (3.7). Note that this function is harmonic and satisfies $\phi_0(\alpha, \beta) = 0$ for $\beta = 2\pi$. Similar to the definition of a new candidate function in (4.4), we define a harmonic function that is related to the $2n$th derivatives of $\phi_0(\alpha, \beta)$ with respect to β, given by

$$\begin{aligned}\phi_{2n}(\alpha, \beta) :=& \frac{2\sqrt{2(\cosh\alpha - \cos\beta)}}{(2n)!}\frac{\partial^{2n}}{\partial\beta^{2n}}\int_0^\infty \tau\frac{\sinh(\theta\tau)\sinh[(2\pi-\beta)\tau]}{\cosh(\pi\tau)\sinh[(\pi-\theta)\tau]}P_{-(1/2)+\mathrm{i}\tau}(\cosh\alpha)\,\mathrm{d}\tau \\ =& \frac{2\sqrt{2(\cosh\alpha - \cos\beta)}}{(2n)!}\int_0^\infty \tau^{2n+1}\frac{\sinh(\theta\tau)\sinh[(2\pi-\beta)\tau]}{\cosh(\pi\tau)\sinh[(\pi-\theta)\tau]}P_{-(1/2)+\mathrm{i}\tau}(\cosh\alpha)\,\mathrm{d}\tau,\end{aligned} \tag{4.6}$$

for $n = 0, 1, \ldots$. These functions are harmonic in the domain D and $\phi_{2n}(\alpha, 2\pi) = 0$, i.e. $\phi_{2n}(\alpha, \beta) = 0$ for $z = 0$, $\xi \geqslant 1$ in a cylindrical coordinate system. Using the new function $\phi_{2n}(\alpha, \beta)$ and a correction function $\psi_{2n}(\alpha, \beta)$ defined in (4.2) with a different kernel,

$$\eta_{2n}(m) = -\frac{2}{\pi}\int_{-\infty}^{0}\frac{\sin(mz)}{m\, I_1(m/\lambda)}\frac{\partial\phi_{2n}}{\partial\xi}(\alpha(1/\lambda, z), \beta(1/\lambda, z))\,\mathrm{d}z, \tag{4.7}$$

the solution for $\Pi(\xi, z)$ is given by the superposition of $F_{2n}(\xi, z) := \phi_{2n}(\alpha(\xi, z), \beta(\xi, z)) + \psi_{2n}(\alpha(\xi, z), \beta(\xi, z))$:

$$\Pi(\xi, z) = -z - \sum_{n=0}^{\infty} A_{2n}\, F_{2n}(\xi, z). \tag{4.8}$$

This expression is similar to (4.5) by Antkowiak *et al.* (2007), except for the different basis functions $F_{2n}(\xi, z)$. The coefficients A_{2n} are determined so that $\Pi(\xi, z) = 0$ on $\mathcal{S}$. After obtaining the coefficients A_{2n} using a collocation method, it is possible to calculate the jet speed. This can be done by considering a derivative with respect to z and the chain rule.

Figure 7 shows contour plots of $F_0(\xi, z)$, $F_2(\xi, z)$ and $F_4(\xi, z)$ for $\lambda = 0.5$ and $H = 1.5$. It can be seen that the higher-order oscillating terms can be included by adding $F_{2n}(\xi, z)$ with a large n. Through a linear combination of F_{2n}, it is possible to extract the solution Π for the boundary value problem (2.6).

4.3. *A semi-analytical solution for a submerged tube*

The same approach can be used to obtain the solution for the problem (2.6) with $h \neq 0$. First, note that $g_\theta(\alpha, \beta)$ defined in (3.8) does not satisfy the boundary condition on the

https://doi.org/10.1017/jfm.2026.11880 Published online by Cambridge University Press

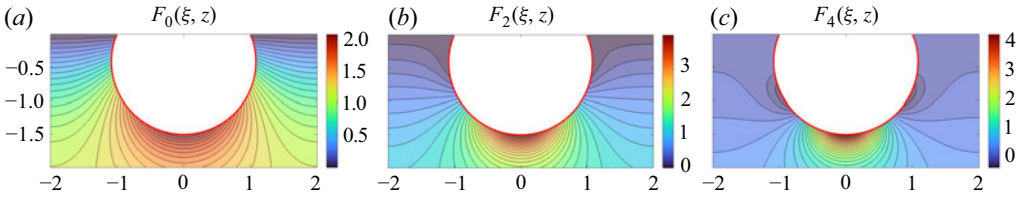


Figure 7. Contour plots of (*a*) $F_0(\xi, z)$, (*b*) $F_2(\xi, z)$ and (*c*) $F_4(\xi, z)$ for $\lambda = 1/2$. Using the superposition of these functions, a solution that satisfies (i)–(v) is constructed.

side of the container. To satisfy the boundary condition, we consider a correction term $\tilde{\phi}_0(\alpha, \beta) := g_\theta(\alpha, \beta)$, and define

$$G(\xi, z) := \tilde{\phi}_0(\alpha(\xi, z), \beta(\xi, z)) + \tilde{\psi}(\alpha(\xi, z), \beta(\xi, z)), \tag{4.9}$$

where $\tilde{\psi}(\xi, z)$ is given by (4.2) in terms of a Fourier–sine series of $\tilde{\phi}_0(\xi, z)$. Using that, the pressure field is given by

$$\Pi(\xi, z) = -z - \sum_{n=0}^{\infty} \tilde{A}_{2n}\, F_{2n}(\xi, z) + h\,(1 - G(\xi, z))\,, \tag{4.10}$$

where the final term captures the boundary condition at $z = 0$ and singularities at $z = 0$, $\xi = \pm 1$. After finding the coefficients $\tilde{A}_{2n}$, it is possible to evaluate the field and velocity of the jets.

For the numerical computation, we truncate the series (4.8) at N to calculate the velocity of jets $v(\theta)$ at the bottom of the bubble. Due to the suitability of the basis in the mixed boundary value problem, the required number of basis functions is small. Similarly to Antkowiak *et al.* (2007), we find that approximately 5–10 bases are sufficient for condition (iv), and absolute error 10^{-4} is obtained. In this paper, eight basis functions are used in all computations. The same number of collocation points is chosen on half of $\mathcal{S}$ to construct the linear system for A_{2n} or $\tilde{A}_{2n}$ to satisfy the boundary condition (iii) in (2.6).

Figure 8 compares the analytical solutions (3.11) and (3.12) for the small-bubble limit, plotted as a black dashed line, and the numerical solutions approximated as a series of basis functions. The accuracy of the analytical solution for the small-bubble limit improves as λ and h decrease. These numerical results indicate that the approximation of the analytical solution derived in (3.11) and (3.12) works well for a wide range of λ and h, especially for small λ and h.

5. Experiment

This section describes the experimental set-up adopted in this work, and compares the experimental results with analytical formulas. The trends of the experimental results are approximated well by the analytical results, i.e. there exists an optimal value to produce high-velocity jets, as shown in figure 6.

5.1. *Experimental set-up*

To produce liquid jets, we follow the example of previous works by Kiyama *et al.* (2016) and Onuki *et al.* (2018), who studied impulse-driven liquid jets produced in a free-falling container. The experimental set-up is shown in figure 9. A test tube (IWAKI, 30 × 200) with inner radius $r^* = 13.5$ mm is filled with silicone oil (Shin-Etsu Silicones, KF-96

https://doi.org/10.1017/jfm.2026.11880 Published online by Cambridge University Press

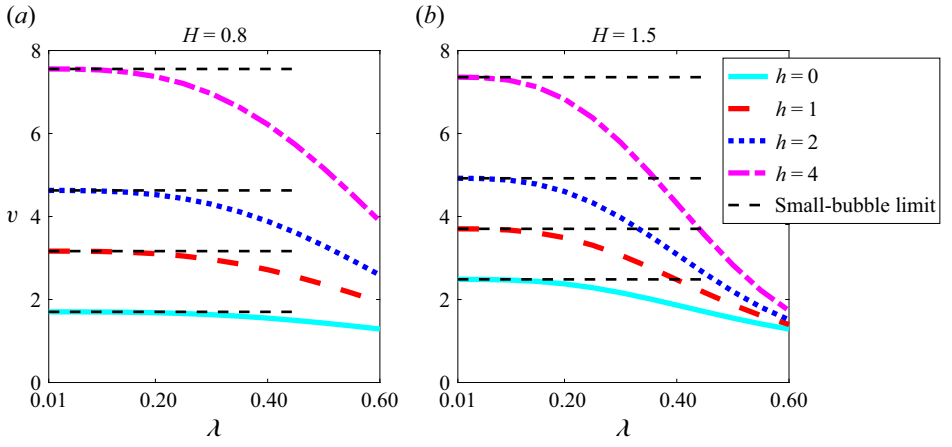


Figure 8. A comparison between the analytical solutions (3.11) and (3.12) for the small-bubble limit plotted as a black dashed line and the numerical solutions calculated as a series of basis functions, for (*a*) $H = 0.8$ and (*b*) $H = 1.5$, with $h = 0$, 1, 2, 4. It can be seen that the accuracy of the analytical solution of the small-bubble limit becomes good as λ and h decrease. The error between the analytical solutions (black dashed lines) and the full solutions (coloured lines) is less than 0.2 % for $H = 0.8$, and less than 0.6 % for $H = 1.5$, when $\lambda = 0.074$.

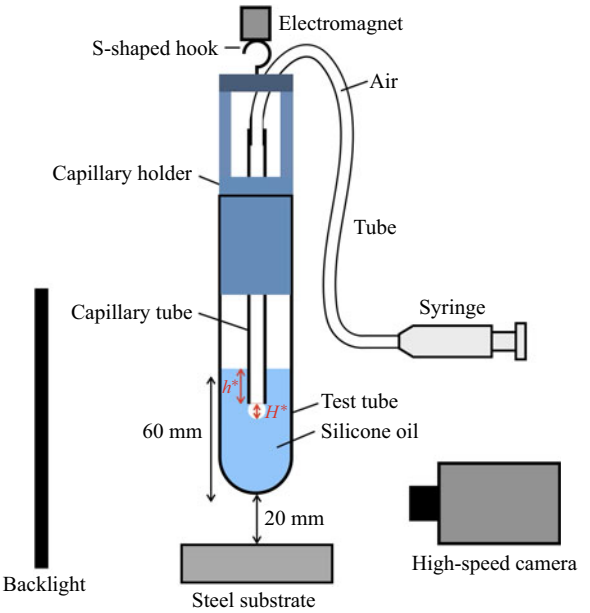


Figure 9. A schematic of the experimental set-up. A container with an inserted capillary tube is fixed above a steel substrate using an electromagnet, and the container is released by switching off the electromagnet to impact the steel substrate. The depth of the bubble H^* is varied by adjusting the pressure inside the capillary tube using a syringe. The bubble and the jet are recorded using a high-speed camera.

series) of kinematic viscosity 10 $\mathrm{mm}^2\ \mathrm{s}^{-1}$ and density 932 $\mathrm{kg\,m}^{-3}$. Silicone oil has a low vapour pressure and is less prone to cavitation, which makes it possible to suppress cavitation-induced effects and isolate the effects of bubble depth and curvature on jet velocity. A glass capillary tube with inner radius $R^* = 1$ mm is inserted into the test tube

https://doi.org/10.1017/jfm.2026.11880 Published online by Cambridge University Press

	Re	We
$h=0$	1.11×10^{2}–8.68×10^{2}	5.70×10^{1}–3.49×10^{3}
$h=2$	4.47×10^{2}–1.43×10^{3}	9.25×10^{2}–9.52×10^{3}
$h=4$	1.09×10^{3}–3.13×10^{3}	5.45×10^{3}–4.54×10^{4}

Table 1. The Reynolds number and Weber number in our experiment.

and firmly fixed using a capillary holder fabricated with a 3-D printer (Bambu Lab A1 3-D printer). A syringe (Terumo, SS-20LZ) is used to connect the container to a small tube, then the bubble is injected into the top of the tube. A steel S-shaped hook is attached to the top of the capillary holder, and the container is suspended above a steel base plate using an electromagnet (Eclipse Magnetics, M52180-12VDC). The distance between the base plate (Toshin Steel, material SS400, thickness $\times$ width $\times$ length are $20\times150\times150\,\mathrm{mm}^3$) and the bottom of the container is 20 mm. When the electromagnet is switched off, the container undergoes free fall and collides with the base plate. Upon impact, the liquid in the container is rapidly accelerated, ejecting a focused jet from an air bubble at the lower end of the capillary. A high-speed camera (Photron, FASTCAM SA-X, 10 000–40 000 fps) with a backlighting set-up (PHLOX, white LED backlight $400\times200\,\mathrm{mm}^2$) is used to record the behaviour of the bubble during the free fall of the container, as well as the jet formation process. The parameter λ, which is the ratio of the radius of the tube to the radius of the container outside the tube, is 0.074 in all experiments. For this λ, it was possible to approximate the jet velocity using the analytical formulas (3.11) and (3.12), as shown in figure 8. The depth of the viscous liquid is set to 60 mm, which is assumed to be much larger than the tube radius. The Reynolds and Weber numbers are calculated using the capillary radius (1 mm) as the characteristic length scale, and the jet velocity as the characteristic velocity. The resulting values are listed in table 1.

Note that the Weber numbers are found to lie in the range 5.70×10^{1}–4.54×10^{4}, with the smallest value still corresponding to $We\gg1$. Following the argument of Gekle & Gordillo (2010), capillary effects are expected to be subdominant during the initial jet formation. Therefore, treating surface tension as a secondary effect in the pressure impulse model is justified for the present parameter range. Nevertheless, surface tension and viscosity may still contribute to the subsequent jet development.

The experimental parameters are h^* and H^*. Three values of h^* are examined: $h^*=0$, 2, 4 mm, which are set based on visual inspection. As H^* oscillates while the tube is falling, a video is captured using a horizontally placed camera. The value of H^* immediately before impact is determined from the recorded images by visual inspection and subsequent analysis using ImageJ. The position of the jet tip generated just after impact is also identified visually, and the jet velocity is then calculated. Experiments are conducted to measure the jet speed as a function of the bubble height H^* and submersion depth h^*.

5.2. *A comparison of the analytical solution with experimental results*

Figure 10 shows image sequences of the jet with different $h=h^*/R^*$ and $H=H^*/R^*$. We set $t=0$ as the time when the container collided with the base. The jet formation process is shown at time intervals 1 ms for $h=0$, 0.5 ms for $h=2$, and 0.3 ms for $h=4$. For each condition, the image sequences in figure 10 also include the spherical bubble shape before the container is released, as well as that during the free fall of the container (25 ms before

https://doi.org/10.1017/jfm.2026.11880 Published online by Cambridge University Press

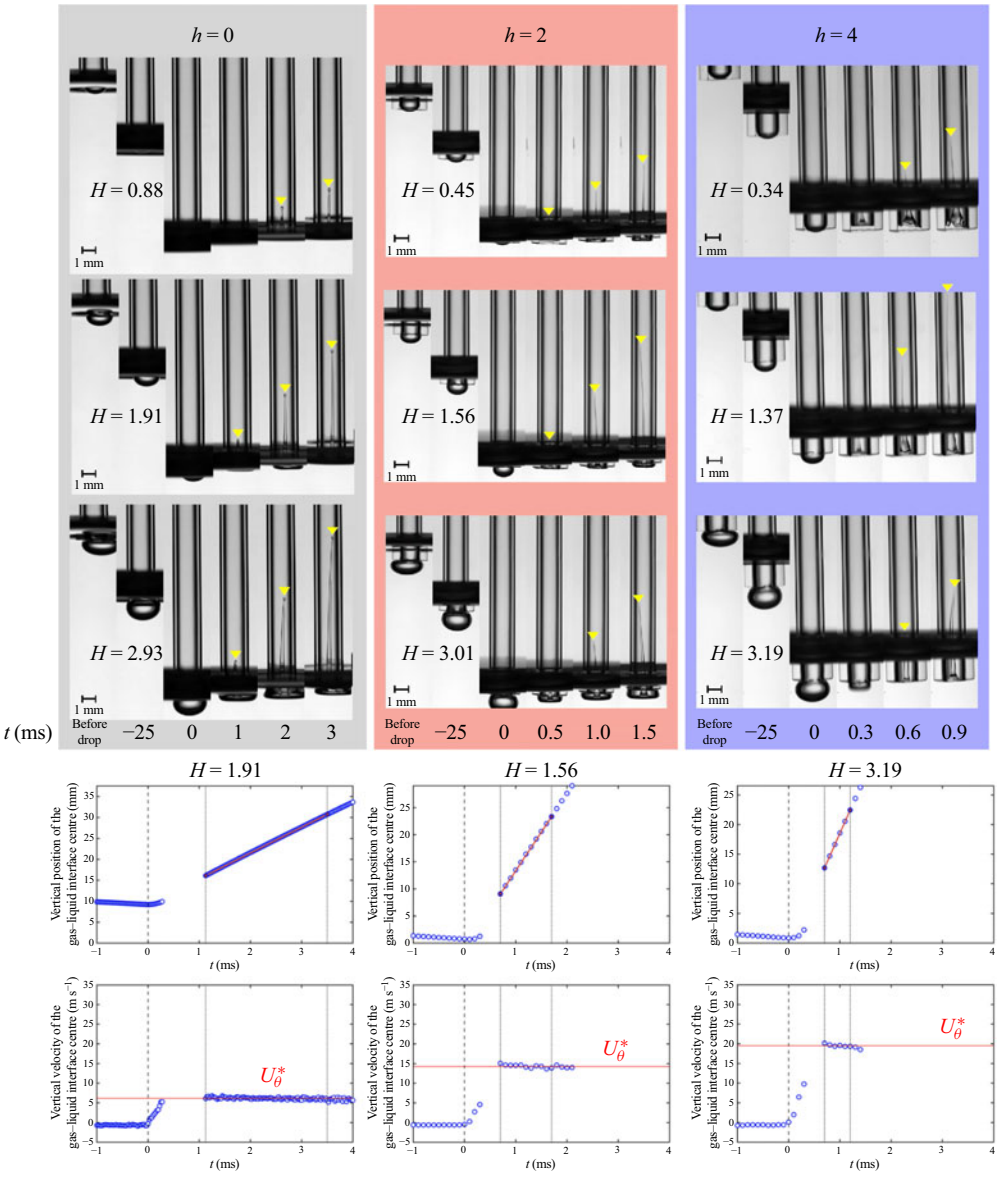


Figure 10. Image sequences of the jet. The moment of impact between the container and the substrate is defined as $t = 0$ ms. For each condition, six images are shown, including images taken before the container is released and 25 ms before impact. The yellow triangles indicate the jet tip position. The bubble grows as the container falls, and becomes nearly spherical. For $h = 0$, the jet velocity increases with increasing H. In contrast, for $h > 0$, there exists a value of H at which the jet velocity reaches a maximum, and this value depends on h. For $h = 2$, the jet velocity is maximised at $H = 1.56$, while for $h = 4$, it reaches a maximum at $H = 1.37$. The positions and velocities of the gas–liquid interface centre are plotted in the bottom panel. A frame rate of 40 000 fps is used for $h = 0$, and 10 000 fps is used for $h = 2$ and $h = 4$. The red lines show the velocity $U^*_\theta(h)$, which is compared with our model given by (3.11) and (3.12).

https://doi.org/10.1017/jfm.2026.11880 Published online by Cambridge University Press

impact). For $h = 0$ and $h = 2$, the bubbles are partially hidden by the interface, making their shapes difficult to observe. Under all conditions, the bubble approaches a nearly spherical, laterally symmetric shape during the free fall of the container. Subsequently, when the container impacts the base plate, the bubble undergoes significant deformation, leading to the ejection of a focused jet. Focusing on the jet tip position at $t = 3$ ms for $h = 0$, it is observed that the jet tip height increases with increasing H. This indicates that for $h = 0$, the jet velocity increases as H increases. In contrast, for $h > 0$, a larger value of H does not necessarily lead to a higher jet tip position. For $h = 2$, the jet tip position at $t = 1.5$ ms shows that the maximum jet height is obtained at $H = 1.56$. Similarly, for $h = 4$, the jet tip position at $t = 0.9$ ms reaches its maximum at $H = 1.37$. These results suggest that for $h > 0$, there exists an optimal value of H at which the jet velocity is maximised, and that this optimal value depends on h.

We calculate the average jet velocity of two time instants, t_0 and t_1. Time t_0 is defined as the moment when the jet tip first forms, while t_1 corresponds to the time at which the jet reaches its maximum observable length within the camera view. The jet tip's positions are measured at these two time points, and the average jet velocity $U^*_\theta(h)$ is then determined from their displacement. The positions and the measured velocity $U^*_\theta(h)$ of the jet tip are shown at the bottom of figure 10.

To fit our analytical solution with the experimental data, we first non-dimensionalised the measured velocity $U^*_\theta(h)$ using the velocity of the container U^*_0 just after impact:

$$U_\theta(h) := \frac{U^*_\theta(h) - U^*_0}{U^*_0}. \tag{5.1}$$

The container experiences free fall before the elastic impact at the bottom. The container velocity U^*_0 is given by $\sqrt{2g^*a^*}$, where a^* represents the container drop height fixed at 20 mm for all experiments, and g^* is the gravitational acceleration. The resulting velocity is $U^*_0 = 0.6241$ m s^{-1}.

Note that our model provides a pressure-impulse-induced initial velocity soon after impact, which differs from the average jet-tip velocity measured in the experiment. To compare the analytical solutions with the experimental data, we considered the following scaling factor $\gamma(h)$, which depends only on the height h:

$$U_\theta(h) \approx \gamma(h)\,(v_f(\theta) + h\, v_g(\theta)). \tag{5.2}$$

The scaling factor represents a physical correction that captures the difference between our model and the measured velocity. The reason why we introduce $\gamma(h)$ is explained in § 6. The value $\gamma(h)$ is determined through fitting of the experimental data using the least squares method. The values of $\gamma(h)$ are 3.143 at $h = 0$, 3.918 at $h = 2$, and 5.615 at $h = 4$.

Figure 11 compares the analytical solution for the small-bubble limit in (3.11) and (3.12), plotted as solid lines, and the experimental data, plotted as dots. Both experimental and analytical data are plotted for $h = 0, 2.0, 4.0$. Each black circle corresponds to a maximum jet velocity in our experiments. Note that when measuring $U^*_\theta(h)$, experimental uncertainties arise from errors of a few (approximately 3) pixels when identifying the jet tip at two time instances. The corresponding uncertainties for $h = 0, 2, 4$ are also shown in figure 11. Although a scaling factor $\gamma(h)$ is needed to fit the experimental data, the trend of the experimental data is approximated well by the analytical solution $v(\theta)$. This indicates that controlling the bubble height H and the submersion depth h is important for producing a high-velocity jet.

https://doi.org/10.1017/jfm.2026.11880 Published online by Cambridge University Press

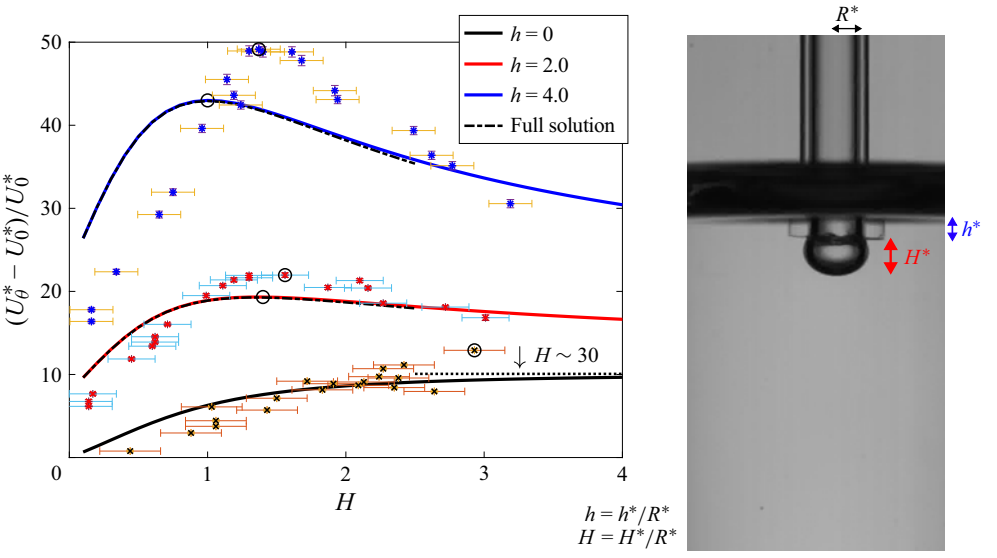


Figure 11. A comparison between the analytical solution for the small-bubble limit in (3.11) and (3.12), plotted as solid lines, and the experimental data, plotted as dots. The ranges of measured jet velocity U_θ^* are 1.11−8.68 m s^{-1} for $h = 0$, 4.47−14.33 m s^{-1} for $h = 2$, and 10.85−31.30 m s^{-1} for $h = 4$. The data are non-dimensionalised by the velocity of the container $U_0^* = 0.6241$ m s^{-1}, and plotted for $h = 0, 2.0, 4.0$. Black circles correspond to the maximum jet velocity in both our theoretical and experimental results. When measuring $U_\theta^*(h)$, experimental uncertainties arise from errors of a few (approximately 3) pixels when identifying the jet tip at two time instances. The corresponding uncertainties for $h = 0, 2, 4$ are also shown. Black dashed lines correspond to the full solution results (4.10) with $\lambda = 0.074$ for $h = 2.0, 4.0$. The full solution is well approximated by the analytical solutions in (3.11) and (3.12).

6. Discussions

This paper has derived an analytical solution for the pressure impulse outside a spherical bubble, generalising previous work by Antkowiak *et al.* (2007). The jet speed is calculated by simple integration of hyperbolic functions, indicating that there exists a maximum jet velocity for a specific bubble height H and submersion depth h.

It should be noted that there is an optimal bubble shape for a submerged tube in a container that produces the fastest jet. This can be explained physically. The total velocity is $v(\theta) = v_f(\theta) + h\, v_g(\theta)$, where $v_f(\theta)$ is a velocity induced by the pressure impulse with $h = 0$ shown in figure 12(*a*), and $v_g(\theta)$ is a velocity due to the height of the liquid in the container in figure 12(*b*). The velocity $v_f(\theta)$ is a monotonically increasing function, because the equicontour line of Π_f is increasingly distorted as the bubble size increases, as shown in figure 12. This produces the large pressure gradient on the bottom of the bubble, and hence the largest jet velocity.

For $v_g(\theta)$, however, our numerical calculation shows that there exists a maximum of $v_g(\theta)$, as shown in figure 12. This can be explained through the analogy of electrical potential. The velocity $v_g(\theta)$ is given by $-\partial g_\theta/\partial z$ with (3.8) evaluated at the bottom. As H becomes large, the bubble can be seen as a sphere with radius $1/\sin(\theta) \to \infty$ and potential 0, attached to the ground with potential 1. This gives us the asymptotic electrical potential as

$$g_\theta(\alpha(\xi, z), \beta(\xi, z)) \sim 1 - \frac{\sin\theta}{\sqrt{\xi^2 + (z - 1/\tan\theta)^2}}, \tag{6.1}$$

https://doi.org/10.1017/jfm.2026.11880 Published online by Cambridge University Press

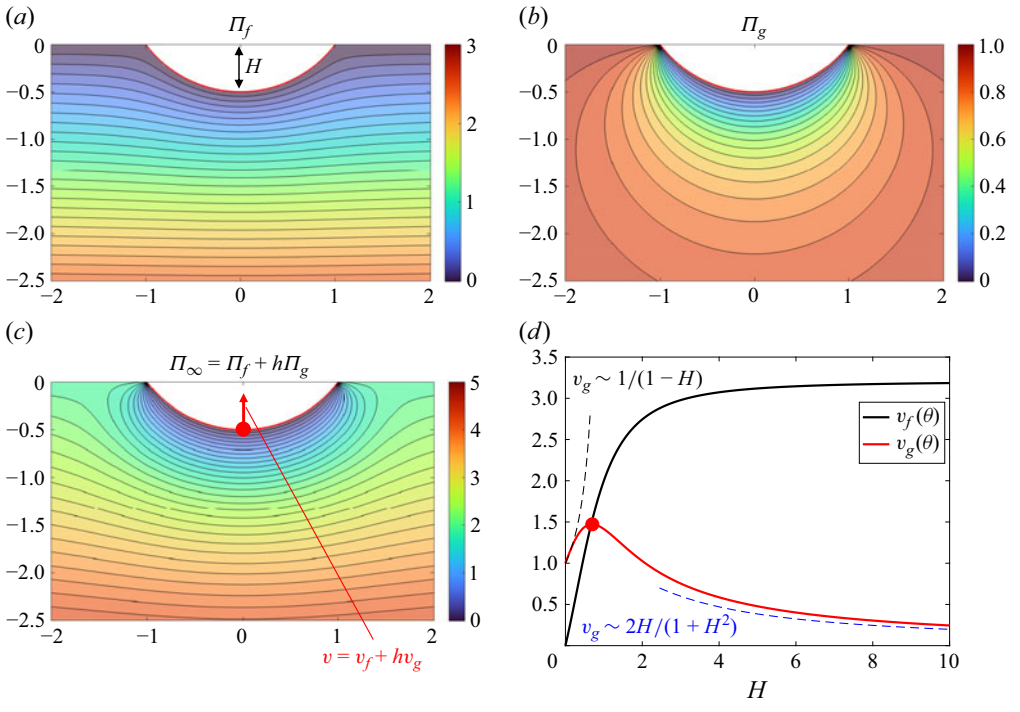


Figure 12. A visual explanation of why the velocity $v(\theta)$ has an optimal value for a specific depth h and bubble height H. The pressure impulse with a submersion depth h is $\Pi_f + \Pi_g \times h$ as shown in (*c*). The velocity v_f induced by Π_f shown in (*a*) is a monotonically increasing function with respect to H, but v_g induced by Π_g shown in (*b*) attains its maximum value at approximately $H = 0.7$. Thus there exists an optimal value for H that maximises the velocity $v(\theta) = v_f(\theta) + h\, v_g(\theta)$ with respect to H as shown in (*d*).

which gives

$$v_g(\theta) = -\frac{\partial g_\theta}{\partial z}(0, \pi + \theta) \sim \frac{2H}{1+H^2}, \tag{6.2}$$

where we used (2.5). This gives the asymptotic behaviour of $v_g(\theta)$ as $H \to \infty$.

For small H, the distance from the top of the bubble to the ground region $z = 0$ gets small as H increases, since the distance is measured as the curved line along electric flux lines. By considering $v_g(0) = 1$ and defining the virtual distance from the bottom of the bubble to the ground as r_v, the velocity v_g is assumed to have an asymptotic behaviour:

$$v_g(\theta) \sim \frac{r_v}{r_v - H} = \frac{1}{1 - H/r_v}. \tag{6.3}$$

Figure 12(*d*) shows two asymptotic behaviours (6.2) and (6.3) with $r_v = 1$ compared with our numerical calculation. These two asymptotics agree well with our numerical calculation of $v_g(\theta)$. Moreover, these behaviours show that there should exist a local maximum for $v_g(\theta)$. The uniqueness of the maximum value has not been proven mathematically. However, from a physical standpoint, as stated above, the velocity $v_g(\theta)$ is expected to decrease monotonically as $H \to \infty$. This is one explanation for why there exists an optimal shape for producing the fastest jet.

The shape of an initial bubble is not perfectly spherical. Therefore, any inclination of the jet may lead to an underestimation of the velocity. Among all experimental conditions,

https://doi.org/10.1017/jfm.2026.11880 Published online by Cambridge University Press

the largest observed inclination of the jet is 3.42° from the vertical, corresponding to a maximum underestimation in jet velocity of approximately 0.178 %.

The jet may also be inclined towards the camera; this inclination cannot be measured from the images. Assuming a maximum inclination 3.42° in this direction, the total error in jet velocity due to such an inclination arising from a non-spherical bubble could reach approximately 0.356 % in our experiments.

The value $\gamma(h)$ fits the difference between the experiments and our mathematical model. The discrepancy between the model and the experiments is attributed mainly to the difference between the pressure-impulse-induced initial velocity predicted by the model and the time-averaged jet-tip velocity measured during the observable jet-elongation stage, as well as to the approximate boundary condition imposed on the pressure impulse at $z = 0$. First, the experimental velocities are effectively time-averaged quantities, whereas the model predicts an instantaneous post-impact velocity. As shown in figure 10, the jet-tip velocity can differ by a factor of approximately 2–4 in the representative cases examined, which explains the discrepancy with the pressure impulse prediction. Second, the model employs an approximate boundary condition for the pressure impulse (2.6) at $z = 0$. Our COMSOL calculations show that this difference introduces an approximately order-one correction factor of 1–1.5 in the examined range, while the overall H-dependence and the position of the maximum remain largely unchanged. In addition, surface tension, viscosity and flow focusing may contribute as secondary effects within the post-impulse regime. To account for these combined effects, we introduce an effective correction factor $\gamma(h)$.

Although our approach works for small λ, a correction term for the analytical solutions (3.7) and (3.8) is necessary for deriving the jet speed when λ is greater than approximately 0.3. In that case, matched asymptotic expansions for the pressure impulse at the outer boundary in the small-bubble limit could provide a promising approach. In general, matched asymptotic expansions match the behaviour of the inner region to that of the outer region, as initially studied by Van Dyke (1975). A review of general perturbation techniques is given in Masoud & Stone (2019). Recently, this approach has been used in various fields of fluid problems, such as to evaluate the evaporation of multiple bubbles (Masoud *et al.* 2021) and slip lengths of superhydrophobic channels. Friction resistances are also approximated well by matched asymptotic expansions; see Miyoshi *et al.* (2024*a*,*b*), Miyoshi & Crowdy (2023) and Rodriguez-Broadbent *et al.* (2024). Future work will focus on this topic to elucidate the effect of side walls to derive another closed-form solution instead of a series solution.

7. Summary

This work has established an expanded analytical framework for the formation of impulse-driven jets from curved fluid interfaces. By solving the pressure impulse problem for spherical bubbles with arbitrary contact angles, we have shown that the jet velocity is governed by the competition between curvature-induced impulse focusing and submersion-induced pressure redistribution. This competition gives rise to an optimal interface geometry that maximises jet speed, providing a clear physical explanation for experimentally observed non-monotonic trends.

Beyond the specific configuration considered here, the present formulation offers a foundation for systematically exploring impulse focusing in more general axisymmetric geometries. The ability to relate interface curvature directly to jet velocity opens a pathway to geometry-controlled jet engineering, such as conical interfaces, with potential implications for high-speed microjet generation, flow focusing devices, and impact-driven injection technologies.

https://doi.org/10.1017/jfm.2026.11880 Published online by Cambridge University Press

Acknowledgements. The first author is supported by a JSPS Postdoctoral Fellowship (JSPS-24KJ0041) and an Excellent Young Researcher Fellowship at the University of Tokyo. This work was supported by JSPS KAKENHI grant no. JP24H00289.

Declaration of interests. The authors report no conflict of interest.

Appendix A. Derivation of the analytical formulas (3.7) and (3.8)

This appendix explains how the 3-D Laplace equations can be solved using a toroidal coordinate system. Following the mathematical set-up provided on p. 222 of Lebedev (1965), we consider a change of variables from cylindrical coordinates (ξ, z) to (α, β):

$$\xi = \frac{\sinh\alpha}{\cosh\alpha - \cos\beta}, \quad z = \frac{\sin\beta}{\cosh\alpha - \cos\beta}, \tag{A1}$$

where the negative semi-infinite region outside the bubble domain is parametrised by

$$0 \leqslant \alpha < \infty, \quad \pi + \theta < \beta \leqslant 2\pi. \tag{A2}$$

Using these new coordinates, the boundary of the spherical bubble $\mathcal{S}$ corresponds to $\beta = \pi + \theta$, and the region $\xi \geqslant 1$ corresponds to $\beta = 2\pi$. The derivatives of the coordinates (α, β) with respect to ξ and z are given by

$$\frac{\partial\alpha}{\partial\xi} = \frac{\xi+1}{z^2+(1+\xi)^2} - \frac{\xi-1}{z^2+(1-\xi)^2}, \quad \frac{\partial\beta}{\partial\xi} = -\frac{4z\xi}{(\xi^2+z^2-1)^2+4z^2} \tag{A3}$$

and

$$\frac{\partial\alpha}{\partial z} = z\left(\frac{1}{z^2+(1+\xi)^2} - \frac{1}{z^2+(1-\xi)^2}\right), \quad \frac{\partial\beta}{\partial z} = \frac{2(\xi^2-z^2-1)}{(\xi^2+z^2-1)^2+4z^2}. \tag{A4}$$

Through direct calculation, we can calculate the metric tensor h_α, h_β and h_φ as

$$h_\alpha = h_\beta = \frac{1}{\cosh\alpha - \cos\beta}, \quad h_\varphi = \frac{\sinh\alpha}{\cosh\alpha - \cos\beta}, \tag{A5}$$

where φ is the azimuthal angle. The 3-D Laplace equation in cylindrical coordinates with a rotational symmetry condition then becomes

$$\frac{\partial}{\partial\alpha}\left(\frac{\sinh\alpha}{\cosh\alpha-\cos\beta}\frac{\partial u}{\partial\alpha}\right) + \frac{\partial}{\partial\beta}\left(\frac{\sinh\alpha}{\cosh\alpha-\cos\beta}\frac{\partial u}{\partial\beta}\right) = 0. \tag{A6}$$

Considering the change of variables $u = \sqrt{2(\cosh\alpha - \cos\beta)}\, v$, we get

$$\frac{\partial^2 v}{\partial\alpha^2} + \frac{\partial^2 v}{\partial\beta^2} + \coth\alpha\,\frac{\partial v}{\partial\alpha} + \frac{1}{4}v = 0. \tag{A7}$$

Now we can use a separation of variables approach. Setting $v = A(\alpha)\,B(\beta)$, we have

$$\begin{cases} \dfrac{\mathrm{d}^2 B}{\mathrm{d}\beta^2} = -\nu^2 B, \\ \dfrac{1}{\sinh\alpha}\dfrac{\mathrm{d}}{\mathrm{d}\alpha}\left(\sinh\alpha\dfrac{\mathrm{d}A}{\mathrm{d}\alpha}\right) - \left(\nu^2 - \dfrac{1}{4}\right)A = 0. \end{cases} \tag{A8}$$

The solution for u can be represented by the superposition of the functions

$$u(\alpha,\beta) = \sqrt{2(\cosh\alpha-\cos\beta)}\,[M_\tau\cosh(\beta\tau) + N_\tau\sinh(\beta\tau)]\,P_{-(1/2)+\mathrm{i}\tau}(\cosh\alpha), \tag{A9}$$

https://doi.org/10.1017/jfm.2026.11880 Published online by Cambridge University Press

where the Legendre function $v = P_\nu(z)$ satisfies

$$(1-z^2)v'' - 2zv' + \nu(\nu+1)v = 0. \tag{A10}$$

To derive the formulas for the pressure impulse (3.7) defined by $f_\theta(\alpha, \beta)$, we follow the procedure in § 8.12 in Lebedev (1965). The boundary condition for the function $f_\theta(\alpha, \beta)$ is given as

$$\left\{ f_\theta(\alpha, \beta) = -z = -\frac{\sin\beta}{\cosh\alpha - \cos\beta} \quad \text{for } \alpha \geqslant 0,\ \ \beta = \pi + \theta, 2\pi. \right. \tag{A11}$$

Note that the condition $f_\theta \to 0$ for $z \to -\infty$ is automatically satisfied by the boundary condition $f_\theta(\alpha, 2\pi) = 0$ as $\alpha \to 0$.

Now we use the property of the Legendre function $P_{-(1/2)+\mathrm{i}\tau}(\cosh\alpha)$ as (Lebedev 1965)

$$\frac{1}{\sqrt{2\cosh\alpha - 2\cos\beta}} = \int_0^\infty \frac{\cosh[(\pi-\beta)\tau]}{\cosh(\pi\tau)} P_{-(1/2)+\mathrm{i}\tau}(\cosh\alpha)\,\mathrm{d}\tau, \tag{A12}$$

and the derivative of (A12) with respect to β is given by

$$-\frac{\sin\beta}{(2\cosh\alpha - 2\cos\beta)^{3/2}} = -\int_0^\infty \tau \frac{\sinh[(\pi-\beta)\tau]}{\cosh(\pi\tau)} P_{-(1/2)+\mathrm{i}\tau}(\cosh\alpha)\,\mathrm{d}\tau. \tag{A13}$$

The left-hand side of (A13) is given by

$$-\frac{\sin\beta}{(2\cosh\alpha - 2\cos\beta)^{3/2}} = 2\frac{f_\theta(\alpha, \beta)}{\sqrt{2(\cosh\alpha - \cos\beta)}} \quad \text{for } \beta = \pi + \theta, 2\pi, \tag{A14}$$

which gives the coefficients of the integrand in (8.12.11) in Lebedev (1965) as

$$\Phi_1 = 0, \quad \Phi_2 = 2\tau \frac{\sinh(\theta\tau)}{\cosh(\pi\tau)}. \tag{A15}$$

Now, by substituting the integrand of (A13) into (8.12.11) with $\beta_1 = 0$ and $\beta_2 = \pi + \theta$, we obtain

$$f_\theta(\alpha, \beta) = 2\sqrt{2(\cosh\alpha - \cos\beta)} \int_0^\infty \tau \frac{\sinh(\theta\tau)\sinh[(2\pi-\beta)\tau]}{\cosh(\pi\tau)\sinh[(\pi-\theta)\tau]} P_{-(1/2)+\mathrm{i}\tau}(\cosh\alpha)\,\mathrm{d}\tau. \tag{A16}$$

Similar manipulation gives the formula for $g_\theta(\alpha, \beta)$ defined in (3.8). Note that the function $g_\theta(\alpha, \beta)$ is derived using the same procedure as in the example on p. 229 of Lebedev (1965), where a boundary condition that has a constant value on the spherical cap is considered.

Note that $\partial\alpha/\partial z = 0$ and

$$\frac{\partial\beta}{\partial z}(0, -H) = \frac{-2(H^2+1)}{(H^2-1)^2 + 4H^2} = -\frac{\sin^2\theta}{1-\cos\theta}. \tag{A17}$$

The derivative with respect to β is

$$\begin{aligned}\frac{\partial f_\theta}{\partial\beta}(\alpha, \beta) = {} & \frac{2\sin\beta}{\sqrt{2(\cosh\alpha - \cos\beta)}} \int_0^\infty \tau \frac{\sinh(\theta\tau)\sinh[(2\pi-\beta)\tau]}{\cosh(\pi\tau)\sinh[(\pi-\theta)\tau]} P_{-(1/2)+\mathrm{i}\tau}(\cosh\alpha)\,\mathrm{d}\tau \\ & - 2\sqrt{2(\cosh\alpha - \cos\beta)} \int_0^\infty \tau^2 \frac{\sinh(\theta\tau)\cosh[(2\pi-\beta)\tau]}{\cosh(\pi\tau)\sinh[(\pi-\theta)\tau]} P_{-(1/2)+\mathrm{i}\tau}(\cosh\alpha)\,\mathrm{d}\tau.\end{aligned} \tag{A18}$$

https://doi.org/10.1017/jfm.2026.11880 Published online by Cambridge University Press

Using $P_{-(1/2)+\mathrm{i}\tau}(1) = 1$, we arrive at

$$\frac{\partial f_\theta}{\partial \beta}(0, \pi + \theta) = \sqrt{\frac{2}{1+\cos\theta}} \int_0^\infty \tau \, \frac{\sinh(\theta\tau)}{\cosh(\pi\tau)} \left(\sin\theta + 2(1+\cos\theta)\tau \, \frac{\cosh[(\pi-\theta)\tau]}{\sinh[(\pi-\theta)\tau]} \right) \mathrm{d}\tau. \tag{A19}$$

Then, using some identities of Legendre function $P_{-(1/2)+\mathrm{i}\tau}$ and its derivative derived from the Mehler–Fock theorem,

$$\frac{\partial f_\theta}{\partial z}(0, \pi + \theta) = \sin^2\left(\frac{\theta}{2}\right) + 8\cos^3\left(\frac{\theta}{2}\right) \int_0^\infty \tau^2 \frac{\sinh(\theta\tau)\cosh[(\pi-\theta)\tau]}{\cosh(\pi\tau)\sinh[(\pi-\theta)\tau]} \, \mathrm{d}\tau. \tag{A20}$$

The derivative of g_θ with respect to z is obtained in a similar manner.

Appendix B. Computation of the Legendre function $P_{-(1/2)+\mathrm{i}\tau}(\cosh\alpha)$

A standard MATLAB platform was used for all numerical computations. However, the original 'legendreP' function in MATLAB does not accept a complex number for the order. It was thus necessary to implement a numerical code to compute $P_{-(1/2)+\mathrm{i}\tau}$.

According to Lebedev (1965), it is known that $P_{-(1/2)+\mathrm{i}\tau}(\cosh\alpha)$ has some integral representations:

$$P_{-(1/2)+\mathrm{i}\tau}(\cosh\alpha) = \frac{2}{\pi}\cosh(\pi\tau) \int_0^\infty \frac{\cos(\tau\theta)}{\sqrt{2\cosh\theta + 2\cosh\alpha}} \, \mathrm{d}\theta. \tag{B1}$$

We observe that the representation (B1) works numerically well for the range $\tau < \tau_0 \in \mathbb{R}$. Although $P_{-(1/2)+\mathrm{i}\tau}(\cosh\alpha)$ is convergent as $\tau \to \infty$, the representation (B1) becomes numerically unstable due to the term $\cosh\pi\tau$ for large τ. For large τ, we use the following representation instead of (B1):

$$P_{-(1/2)+\mathrm{i}\tau}(\cosh\alpha) = \frac{2}{\pi\tanh(\pi\tau)} \int_\alpha^\infty \frac{\sin(\tau\theta)}{\sqrt{2\cosh\theta - 2\cosh\alpha}} \, \mathrm{d}\theta. \tag{B2}$$

Note that the representation (B2) becomes numerically unstable for small τ due to the term $1/\tanh(\pi\tau)$. The derivative of $P_{-(1/2)+\mathrm{i}\tau}(\cosh\alpha)$ with respect to α is calculated using the derivative of the integrand of (B1). For all numerical calculations, we use a fixed value $\tau_0 = 3$. Note that for $\alpha = 0$, it is easy to see that $P_{-(1/2)+\mathrm{i}\tau}(1) = 1$.

References

Andrade, K., Catalán, J., Marín, J.F., Salinas, V., Castillo, G., Gordillo, L. & Gutiérrez, P. 2023 Swirling fluid reduces the bounce of partially filled containers. *Phys. Rev. Lett.* **130** (24), 244001.

Antkowiak, A., Bremond, N., Le Dizès, S. & Villermaux, E. 2007 Short-term dynamics of a density interface following an impact. *J. Fluid Mech.* **577**, 241–250.

Bartolo, D., Josserand, C. & Bonn, D. 2006 Singular jets and bubbles in drop impact. *Phys. Rev. Lett.* **96** (12), 124501.

Batchelor, G.K. 2000 *An Introduction to Fluid Dynamics*. Cambridge University Press.

Baxter, J. & Mitragotri, S. 2006 Needle-free liquid jet injections: mechanisms and applications. *Expert Rev. Med. Devices* **3** (5), 565–574.

Cheng, X., Chen, X.-P., Ding, H., Zhang, C.-Y., Hu, H. & Jia, L. 2024 Viscous influences on impulsively generated focused jets. *Phys. Rev. Fluids* **9** (8), L082001.

Dixit, A., Oratis, A., Zinelis, K., Lohse, D. & Sanjay, V. 2025 Viscoelastic Worthington jets and droplets produced by bursting bubbles. *J. Fluid Mech.* **1010**, A2.

Dombrovsky, L.A., Levashov, V.Y., Shoval, S. & Bormashenko, E. 2025 Progress in understanding of evaporation of droplets: fundamentals and applications. *Adv. Colloid Interface Sci.* **344**, 103605.

Eggers, J. & Villermaux, E. 2008 Physics of liquid jets. *Rep. Prog. Phys.* **71** (3), 036601.

Gekle, S. & Gordillo, J.M. 2010 Generation and breakup of Worthington jets after cavity collapse. Part 1. Jet formation. *J. Fluid Mech.* **663**, 293–330.

https://doi.org/10.1017/jfm.2026.11880 Published online by Cambridge University Press

GEKLE, S., GORDILLO, J.M., VAN DER MEER, D. & LOHSE, D. 2009 High-speed jet formation after solid object impact. *Phys. Rev. Lett.* **102** (3), 034502.
GORDILLO, J.M. & BLANCO-RODRÍGUEZ, F.J. 2023 Theory of the jets ejected after the inertial collapse of cavities with applications to bubble bursting jets. *Phys. Rev. Fluids* **8** (7), 073606.
GORDILLO, J.M., ONUKI, H. & TAGAWA, Y. 2020 Impulsive generation of jets by flow focusing. *J. Fluid Mech.* **894**, A3.
KAMAMOTO, K., ONUKI, H. & TAGAWA, Y. 2021 Drop-on-demand painting of highly viscous liquids. *Flow* **1**, E6.
KIYAMA, A., TAGAWA, Y., ANDO, K. & KAMEDA, M. 2016 Effects of a water hammer and cavitation on jet formation in a test tube. *J. Fluid Mech.* **787**, 224–236.
KOBAYASHI, K., WATANABE, H., YEE, J., TORII, S., KURITA, M. & TAGAWA, Y. 2024 Development and evaluation of on-demand printing technology for highly viscous liquids. *J. Imaging Soc. Japan* **63** (5), 014035.
KRISHNAN, S., BHARADWAJ, S.V. & VASAN, V. 2022 Impact of freely falling liquid containers and subsequent jetting. *Exp. Fluids* **63** (7), 108.
KURIHARA, C., KIYAMA, A. & TAGAWA, Y. 2025 Pressure fluctuations of liquids under short-time acceleration. *J. Fluid Mech.* **1003**, A20.
LEBEDEV, N.N. 1965 *Special Functions and their Applications*. Prentice-Hall, Inc.
LOHSE, D. 2022 Fundamental fluid dynamics challenges in inkjet printing. *Annu. Rev. Fluid Mech.* **54** (1), 349–382.
MASOUD, H., HOWELL, P.D. & STONE, H.A. 2021 Evaporation of multiple droplets. *J. Fluid Mech.* **927** (4), R4.
MASOUD, H. & STONE, H.A. 2019 The reciprocal theorem in fluid dynamics and transport phenomena. *J. Fluid Mech.* **879**, P1.
MIYOSHI, H. & CROWDY, D.G. 2023 Estimating conformal capacity using asymptotic matching. *IMA J. Appl. Math.* **88** (3), 472–497.
MIYOSHI, H., KIRK, T.L., HODES, M. & CROWDY, D.G. 2024*a* Fully developed flow through shrouded-fin arrays: exact and asymptotic solutions. *J. Fluid Mech.* **991**, A2.
MIYOSHI, H., RODRIGUEZ-BROADBENT, H. & CROWDY, D.G. 2024*b* Numerical validation of analytical formulas for channel flows over liquid-infused surfaces. *J. Engng Math.* **144** (1), 14.
MOHIZIN, A. & KIM, J.K. 2023 Conceptualisation of a novel electromechanical system for small-volume needle-free jet injection. *Engng Appl. Comput. Fluid Mech.* **17** (1), 2240868.
ONUKI, H., OI, Y. & TAGAWA, Y. 2018 Microjet generator for highly viscous fluids. *Phys. Rev. Appl.* **9** (1), 014035.
PHILIPPI, J., ANTKOWIAK, A. & LAGRÉE, P.-Y. 2018 A pressure impulse theory for hemispherical liquid impact problems. *Eur. J. Mech. B/Fluids* **67**, 417–426.
POPOV, Y.O. 2005 Evaporative deposition patterns: spatial dimensions of the deposit. *Phys. Rev. E* **71** (3), 036313.
REUTER, F. & OHL, C.-D. 2021 Supersonic needle-jet generation with single cavitation bubbles. *Appl. Phys. Lett.* **118** (13), 134103.
RODRIGUEZ-BROADBENT, H., MIYOSHI, H. & CROWDY, D.G. 2024 Asymptotically exact formulas for channel flows over liquid-infused surfaces. *IMA J. Appl. Math.* **89**, 623–660.
ROHILLA, P. & MARSTON, J. 2023 Focused, high-speed liquid jets induced via low-voltage sparks in capillary tubes. *Exp. Fluids* **64** (5), 90.
SRIVASTAVA, A., KUNDU, A. & PAUL, A.R. 2025 A detailed review of the recent development of needle-free drug delivery devices. *J. Med. Engng Technol.* **49** (6), 187–206.
TAGAWA, Y., OUDALOV, N., VISSER, C.W., PETERS, I.R., VAN DER MEER, D., SUN, C., PROSPERETTI, A. & LOHSE, D. 2012 Highly focused supersonic microjets. *Phys. Rev. X* **2** (3), 031002.
VAN DYKE, M. 1975 Perturbation methods in fluid mechanics/annotated edition. *NASA STI/Recon Tech. Rep. A* **75**, 46926.
WATANABE, H., KUSUNO, H. & TAGAWA, Y. 2025 Effect of a converging container shape on the velocity of an impact-induced focused liquid jet. *Intl J. Multiphase Flow* **193**, 105348.
WILSON, S.K. & D'AMBROSIO, H.-M. 2023 Evaporation of sessile droplets. *Annu. Rev. Fluid Mech.* **55**, 481–509.
XIE, W. 2025 Preliminary semi-analytical investigation of momentum exchange in a bouncing container filled with swirling fluid: pressure impulse induced by central jet. *Mech. Res. Commun.* **144**, 104380.

https://doi.org/10.1017/jfm.2026.11880 Published online by Cambridge University Press